



**HAL**  
open science

## Tomographic Reconstruction of 3D Objects using Marked Point Process Framework

Riadh Ben Salah, Olivier Alata, Benoit Tremblais, Lionel Thomas, Laurent  
David

► **To cite this version:**

Riadh Ben Salah, Olivier Alata, Benoit Tremblais, Lionel Thomas, Laurent David. Tomographic Reconstruction of 3D Objects using Marked Point Process Framework. *Journal of Mathematical Imaging and Vision*, 2018, 60 (7), pp.1132-1149. 10.1007/s10851-018-0800-6 . ujm-03840033

**HAL Id: ujm-03840033**

**<https://ujm.hal.science/ujm-03840033>**

Submitted on 4 Nov 2022

**HAL** is a multi-disciplinary open access archive for the deposit and dissemination of scientific research documents, whether they are published or not. The documents may come from teaching and research institutions in France or abroad, or from public or private research centers.

L'archive ouverte pluridisciplinaire **HAL**, est destinée au dépôt et à la diffusion de documents scientifiques de niveau recherche, publiés ou non, émanant des établissements d'enseignement et de recherche français ou étrangers, des laboratoires publics ou privés.

# Tomographic Reconstruction of 3D Objects using Marked Point Process Framework

Riadh Ben Salah · Olivier Alata · Benoit Tremblais · Lionel Thomas · Laurent David

Received: November 2016 / Accepted: date

**Abstract** For reconstructing sparse volumes of 3D objects from projection images taken from different viewing directions, several volumetric reconstruction techniques are available. Most popular volume reconstruction methods are algebraic algorithms (e.g. the multiplicative algebraic reconstruction technique, MART). These methods which belong to voxel-oriented class, allows volume to be reconstructed by computing each voxel intensity. A new class of tomographic reconstruction methods, called “object-oriented” approach, has recently emerged and was used in the Tomographic Particle Image Velocimetry technique (Tomo-PIV). In this paper, we propose an object-oriented approach, called IOD-OVRMPP (Iterative Object Detection - Object Volume Reconstruction based on Marked Point Process), to reconstruct the volume of 3D objects from projection images of 2D objects. Our approach allows the

problem to be solved in a parsimonious way by minimizing an energy function based on a least squares criterion. Each object belonging to 2D or 3D space is identified by its continuous position and a set of features (marks). In order to optimize the population of objects, we use a simulated annealing algorithm which provides a “Maximum A Posteriori” (MAP) estimation. To test our approach, we apply it to the field of Tomo-PIV where the volume reconstruction process is one of the most important steps in the analysis of volumetric flow. Finally, using synthetic data, we show that the proposed approach is able to reconstruct densely seeded flows.

**Keywords** 3D Object Reconstruction · Stochastic Models · Marked Point Processes · Metropolis-Hastings-Green (MHG) algorithm · Simulated annealing · Tomographic PIV

---

Riadh Ben Salah  
Laboratoire Hubert Curien, Université de Lyon, UJM-Saint-Etienne, CNRS UMR 5516, IOGS, F-42023, Saint-Etienne, France E-mail: riadhbs@yahoo.com

Olivier Alata  
Laboratoire Hubert Curien, Université de Lyon, UJM-Saint-Etienne, CNRS UMR 5516, IOGS, F-42023, Saint-Etienne, France E-mail: olivier.alata@univ-st-etienne.fr

Benoit Tremblais  
Laboratoire XLIM, Axe ASALI/SRI, CNRS 7252, Université de Poitiers, France  
E-mail: benoit.tremblais@univ-poitiers.fr

Lionel Thomas  
Institut P', UPR 3346, CNRS-Université de Poitiers-ENSMA, France  
E-mail: lionel.thomas@univ-poitiers.fr

Laurent David  
Institut P', UPR 3346, CNRS-Université de Poitiers-ENSMA, France  
E-mail: laurent.david@univ-poitiers.fr

## 1 Introduction and Motivation

In the 80s, tomographic reconstruction methods were generally classified into two categories: analytical methods [14] and algebraic methods [38]. Analytical methods are fast and simple to implement. They give high quality reconstruction results only if the trajectory acquisition is full with a good sampling of projection images. However, with a limited number of views or noisy images, these methods perform poorly. In this case, it is better to use algebraic methods which adopt a discrete approach to the problem. Algebraic methods assume that the physical volume to reconstruct is sampled on a regular 3d grid. Thus, the volume is formed of voxels with unknown values. The assumption is that each detected value in a pixel from projection images is a linear combination of voxel values. This physically means that

each voxel contributes (possibly with a zero coefficient) to each line of sight.

The estimation of the volume intersection can be readily performed assuming voxels as cubes or spheres. In this formulation, the problem involves solving the system  $P = Rf$ , where  $P$  is a vector containing the set of projection images,  $f$  is a vector containing the voxel values of the volume to reconstruct and  $R$  is a matrix of coefficients of intersection that links  $P$  to  $f$ . An attempt could be made to solve the system using the generalized inverse of  $R$ :  $f = (R^t R)^{-1} R^t P$ . However, this inverse problem admits no solution because  $P$  is noisy (measurement noise, gap between the model and the data, etc.). The resolution of this “ill-posed problem” [31] can be achieved by using iterative tomographic reconstruction methods like algebraic approaches.

Algebraic methods were introduced by Kaczmarz [35]. The leader of this family of algorithms is the ART method (Algebraic Reconstruction Technique) [29]. Many other algebraic methods were proposed like MART (Multiplicative ART) [32], AART (Adaptive ART) [40], SIRT (Simultaneous Iterative Reconstruction Technique) [12], SART (Simultaneous ART) [3] and SMART (Simultaneous MART) [19,53]. Later, methods based on reconstruction by blocks, such as BIMART (Block Iterative MART), were introduced by Charles Byrne [13].

Algebraic methods allow the introduction of some constraints on the solution like the geometry of the acquisition system. Unfortunately, they converge, most of the time, to least squares solutions, which suppose Gaussian noise on the data. To tackle these problems, statistical methods were proposed. They consider  $P$ , and sometimes  $f$ , as random variables, to which a probability distribution reflecting uncertainty in the data (noise, modeling error) and  $f$  (in the case of Bayesian methods) are assigned [49]. The best known statistical method is called MLEM (Maximum Likelihood Expectation Maximization) and was developed in 1982 by Shepp and Vardi [54]. The MLEM method is a special case of the more general approach called Expectation Maximization (EM) [21]. An accelerated version of MLEM, called OSEM (Ordered Subsets Expectation Maximization) [34], was also proposed. Many other statistical methods were also developed like GC (Conjugate Gradient) [36], MENT (Maximum Entropy) [44] and MEM (Maximum Entropy on the Mean) [51,27]. Both statistical and algebraic methods are discrete tomographic reconstruction methods.

Recently, existent tomographic reconstruction methods were applied in the fluid mechanics domain to reconstruct 3D particle volumes from a set of particle images. The images are acquired with a 3D tomographic

optical system called Tomographic Particle Image Velocimetry (Tomo-PIV) which was introduced by Elsinga et al [26].

The principle of the Tomo-PIV is based on the computation of the velocity vector field of a flow from the displacement of the particles recorded on several images. Particles are seeded in the flow and are illuminated by a thick laser sheet which defines the volume of interest. The light scattered by the particles is captured by several high-resolution digital cameras from different viewing angles (usually 4 - see Fig.1). The information on the line of sight of each pixel in a camera, throughout the examined volume, is described by a polynomial approximation made from a 3D calibration procedure. Thus, the projection images set captured at a given time is supplied to a 3D tomographic reconstruction algorithm to reconstruct a volume of 3D particles.

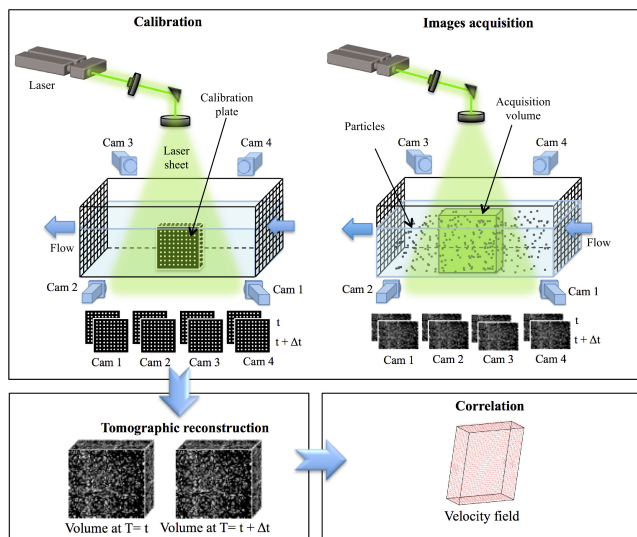


Fig. 1 Tomo-PIV principle.

Finally, the sequences of 3D particle volumes are used to estimate the sequences of velocity fields using advanced cross-correlation techniques. The problem of tomographic reconstruction in the Tomo-PIV field is different than in other domains for the following reasons:

- The volume of interest is composed of 3D particles with a high density level (up to 800,000 particles);
- The presence of ghost particles (artifacts) in reconstructed volumes due to the limited number of views (usually 4 cameras);
- The experimental projection image size can reach  $4000 \times 4000$  pixels (volume size of  $4000 \times 4000 \times 400$  voxels for example);
- Noisy data due to the complex installation and vibration of the acquisition system.

In such a context, the discrete tomographic reconstruction methods proposed to solve the specific problem of TomoPIV can be divided into two classes. The first class is called fast methods and it covers algorithms designed to reduce the computational costs and accelerate the convergence to a solution by estimating the initial volume intensity distribution. The study conducted by Worth and Nickels [65] which yielded an approach named MFG (Multiplicative First Guess) can be mentioned. Atkinson and Soria [4] developed the MLOS (Multiplicative Line Of Sight) method to accelerate the MART method which is the most widely used algebraic technique in the Tomo-PIV field [20,58]. Maas & al. [42] proposed the MinLOS (Minimum Line Of Sight) method which is a variant of MLOS. In the same context, other methods were developed like SAPIV (Synthetic Aperture Particle Image Velocimetry) [7], MG (Multi-Grid) [23] and VS-TPIV (Volume Segmentation - Tomographic Particle Image Velocimetry) [66]. The second class is based on sparse models. In this class, the problem of tomographic reconstruction was treated in a framework exploiting the sparsity of the volume as in methods based on the  $L_1$  norm [24] and others based on basis-pursuit algorithms [48,33].

Analytical and discrete tomographic reconstruction methods called “voxel oriented” methods are based on the calculation of the intensity of each voxel in the volume [8]. They take up a lot in memory storage and do not take sufficiently into account the particular shape of the objects to be reconstructed.

To tackle these problems, “object-oriented” methods, have emerged [64,15,8]. Methods belonging to this category were developed in the fluid mechanics domain. The proposed solutions are based on the parsimony of volumes: they consider the volume as a set of 3D objects. The objects represent 3D particles which are identified by their positions and features. In 2012, Wieneke [64] proposed an algorithm called IPR (Iterative Particle Reconstruction) to reconstruct 3D-particle locations by comparing the recorded images with generated ones calculated from the particle distribution in the volume. In 2014, Champagnat et al. proposed the PVR (Particle Volume Reconstruction) method [15]. This approach is a combination between an “object-oriented” approach and algebraic methods (MART, SMART). The results obtained with numerical simulations showed that the proposed methods give equivalent reconstruction quality to the MART method for very high particle seeding density. However, proposed “object-oriented” methods are very specific to Tomo-PIV problems and cannot be exploited in other fields using sparse volumes.

In this paper, we present a general “object-oriented” approach to reconstruct volumes of 3D objects. The

proposed approach can be used in several areas and meets the following criteria:

- It exploits the parsimony of the volumes using an appropriate mathematical formalism;
- It allows *a priori* information to be easily introduced;
- It works with real-space coordinates in order to locate the objects with high accuracy;
- It solves an ill-posed problem even in the case of very high densities of objects;
- It improves the reconstruction quality with respect to state-of-the-art ART methods and reduces memory usage as well as the artifact rate by using a formalism suited to the problem addressed.

This paper focuses on the reconstruction of volumes of 3D objects in large configuration spaces, formulated in a marked point process reconstruction framework.

Stochastic models based on marked point processes have been used in various application domains, from 3D reconstruction to texture modeling such as the reconstruction of buildings [45] or vascular trees [57], and the detection of tree crowns [46], populations of birds [22] or road networks [59]. These models have proved their efficiency for object extraction in large sample spaces.

Considering previously published papers [9,10], it provides additional details and newer contributions:

- We introduce a general framework in order to make geometrical object reconstruction based on marked point processes using a minimum mean square error estimation criterion.
- As one of the main objectives of Tomo-PIV is to reconstruct a velocity field using two consecutive volumes, a comparison is made on this topic between the proposed method and an optimized MinLOS-MART (Minimum Line-Of-Sight, Multiplicative Algebraic Reconstruction Technique) algorithm [58] for synthetic data.

It should be noted that we have not provided our results on experimental data but these can be found in [11].

This paper is organized as follows: in section 2, after a quick introduction on marked point processes, we present the general formalism of the reconstruction method, called IOD-OVRMPP (Iterative Object Detection - Object Volume Reconstruction based on Marked Point Process) and we show how to simulate it. In section 3, we present an application of our approach to reconstruct a population of 3D particles. We compare it to the reference algebraic reconstruction technique, MinLOS-MART, using synthetic data with different seeding densities. Finally in section 4, the ma-

for findings are summarized, some concluding remarks made and some perspectives given.

## 2 Object reconstruction based on marked point processes

### 2.1 Definitions

In this section, the basic ideas of point processes (PP) and marked PP (MPP) are recalled [61,18]. A MPP provides a naturally sparse representation of configurations of geometrical objects of interest which are inside a considered continuous space. They allow the physical process to be better approximated by a disconnection from the numerical model induced by a regular sampling grid (pixels in image or voxels in volume).

Let  $K \subset \mathbb{R}^d$  ( $d = 2$  or  $3$  in this paper) be a compact subset with  $0 < \nu(K) < \infty$ ,  $\nu$  a Borel measure. A realization of a PP on  $K$  is a finite configuration of points  $\{k_i \in K, i = 1, \dots, N\}$  as  $k_i \neq k_j$  for  $i \neq j$ . To form more complex objects, a geometrical mark can be attached to each point, like a radius for example. In that case, a configuration of circles whose points  $\{k_i, i = 1, \dots, N\}$  are the centers is obtained. Let  $(M, \mathcal{M}, P_M)$  be the probability space which describes the marks ( $M \subset \mathbb{R}^+$  for a radius). A finite random configuration of marked points (or objects) is a sample of a MPP if only the position process of objects is a PP. Based on this definition, volume or image geometrical features are viewed as a set of objects identified jointly by their positions in the image and their geometrical characteristics (the marks).

The simplest MPP is the homogeneous Poisson MPP. That is to say, the number of points in each  $A \subset K$  has a Poisson distribution with mean  $\nu(A) = \beta\mu(A)$ , with  $\mu$  the Lebesgue measure, and the points representing the positions of the objects are uniformly and independently distributed in  $K$ . The marks are chosen independently in  $M$  for each point. For a more complete presentation of MPP, the reader is referred to [55,16].

Let us define a configuration of marked points by  $y = \{(k_1, m_1), \dots, (k_N, m_{n(y)})\}$ , where  $k_i \in K$  and  $m_i \in M$ ,  $i = 1, \dots, n(y)$  denote the object positions and the object marks respectively.  $n(y)$  is the number of marked points in the configuration  $y$ . A configuration of a MPP is classically viewed as a sample issued from an unnormalized probability density  $f$  (as the normalizing constant is intractable) which is a Gibbs distribution:

$$f(y|\theta) \propto \exp(-U(y|\theta)) \quad (1)$$

with  $\theta$  a set of parameters. The energy  $U(y|\theta)$  allows the properties of configuration  $y$  to be modeled and is composed of the sum of two terms: 1) a data-driven

energy or external energy denoted  $U_{\text{ext}}(y|\theta_{\text{ext}})$  that reflects the adequacy between configurations of objects and the observed data and 2) an internal energy denoted  $U_{\text{int}}(y|\theta_{\text{int}})$  that reflects an *a priori* on such configurations. This leads to the following expression:

$$U(y|\theta) = U_{\text{ext}}(y|\theta_{\text{ext}}) + U_{\text{int}}(y|\theta_{\text{int}}) \quad (2)$$

and  $\theta = \theta_{\text{ext}} \cup \theta_{\text{int}}$ . Thus, for a given value of  $\theta$ , the most likely configurations correspond to the ones that have the global minimum of the total energy:

$$\hat{y} = \underset{y}{\operatorname{argmin}} U(y|\theta) \quad (3)$$

The computation of the global minimum of the energy is classically performed by a simulated annealing which is a stochastic method of optimization (see [28, 5] and section 2.3).

An appropriate definition of the data energy allows marked points (objects) that are consistent with respect to a given observation to be obtained. For Tomo-PIV, the process must converge to an appropriate configuration of 2D or 3D objects with respect to the projection images.

### 2.2 Energy of marked point process

#### 2.2.1 Data-driven energy

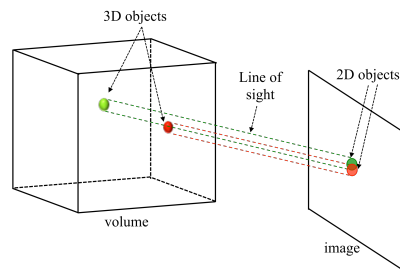


**Fig. 2** Overlapping of two 2D objects issued from the projection of two separate 3D objects, located on the same line of sight.

This section presents our main theoretical contribution in object reconstruction based on MPP: a data-driven energy derived from a minimum mean square error (MMSE) criterion. In this paper, the data-driven energy will be used to search 2D objects in projection images ( $K \subset \mathbb{R}^2$ ) or to reconstruct 3D objects in a volume ( $K \subset \mathbb{R}^3$ ), from projection images. In both cases, it is computed thanks to the intensity of 2D objects in projection images. Its definition takes into account a

possible interaction of objects when associated geometrical marks overlap (see Fig. 2). Let us notice that previously defined MPP in a context of image processing never introduce an interaction in the data-driven term: the interactions between objects are defined inside the internal term [55, 56, 16, 2]. In [43], the MMSE is already used to define the data-driven energy of the proposed MPP but the contribution of each marked point and their interaction terms are not developed.

The mean square error (MSE) of a configuration  $y$  knowing an observation set  $o = \{o_s\}_{s \in S}$  can be written as follows:

$$MSE(y|o) = \sum_{s \in S} (o_s - p_s)^2 \quad (4)$$

$S$  represents the set of sites and  $p_s$  the reconstructed value in  $s$  by the configuration  $y$ :

$$p_s = \sum_{y_j, y_j \rightarrow s} p_{y_j \rightarrow s} \quad (5)$$

Thus,  $p_s$  is the sum of the contributions of each object  $y_j \in y$  which has a non-zero intensity at site  $s$ . This property will be denoted  $y_j \rightarrow s$  and  $p_{y_j \rightarrow s}$  is the intensity generated by  $y_j$  at site  $s$  (see Sections 1 and 3.1 for discretization procedure and objects used in Tomo-PIV). Equation 5 also implies that objects have a finite extension (associated to the chosen geometrical marks) and they do not therefore provide intensity all over the sites.

In view of these considerations, a neighboring relationship between two objects can be defined as follows:

$$y_j \overset{\circ}{\sim} y_k \text{ if } \exists s \in S \text{ s.t. } y_j \rightarrow s \text{ and } y_k \rightarrow s \quad (6)$$

The development of  $MSE(y|o)$  (Eq. 4) and the deletion of constant terms (computation details can be found in **Appendix A**) allow the expression of a data-driven energy in the form of a sum of two energies  $U_{\text{ext},1}(y|\theta_{\text{ext}}) + U_{\text{ext},2}(y|\theta_{\text{ext}})$  to be obtained:

$$U_{\text{ext},1}(y|\theta_{\text{ext}}) = \sum_{y_j \in y} \phi_{\text{ext},1}(y_j) \quad (7)$$

where

$$\phi_{\text{ext},1}(y_j) = \sum_{s \in S, y_j \rightarrow s} p_{y_j \rightarrow s} (p_{y_j \rightarrow s} - 2o_s) \quad (8)$$

and

$$U_{\text{ext},2}(y|\theta_{\text{ext}}) = \sum_{y_j \overset{\circ}{\sim} y_k, j < k} \phi_{\text{ext},2}(y_j, y_k) \quad (9)$$

where

$$\phi_{\text{ext},2}(y_j, y_k) = \sum_{s \in S, y_j \rightarrow s \ \& \ y_k \rightarrow s} 2p_{y_j \rightarrow s} p_{y_k \rightarrow s} \quad (10)$$

By considering Equations (8) and (10), the data-driven energy can be written:

$$U_{\text{ext}}(y) = \sum_{y_j \in y} \phi_{\text{ext},1}(y_j) + \sum_{\substack{y_j, y_k, j < k \\ y_j \overset{\circ}{\sim} y_k}} \phi_{\text{ext},2}(y_j, y_k) \quad (11)$$

The first-order term,  $\phi_{\text{ext},1}$ , contains a correlation operator between the values generated by an object and the values at its corresponding locations in the observed data. If  $\phi_{\text{ext},1}(y_j) < 0$ , the object  $y_j$  is attractive and its presence allows the global energy of the system to be minimized. Conversely, if  $\phi_{\text{ext},1}(y_j) > 0$ , the object  $y_j$  will be penalized. Then,  $U_{\text{ext},1}$  allows the creation of objects in regions with high intensities in observed images. Note that since some objects are attractive, it is necessary to have an exclusionary term to avoid the accumulation of objects in the final configuration. It is the role of the second-order term  $U_{\text{ext},2}$ . Thus, this energy is based on the neighborhood relationship  $\overset{\circ}{\sim}$  (see Eq. 6) that occurs between two objects when their projections overlap (Fig. 2): function  $\phi_{\text{ext},2}$  acts as a correlation operator on the intersection of objects. It is important to note that its computation depends on the spatial extension of the projections of objects and their non-zero overlaps.

To sum up, for a given object  $y_j$ ,  $\phi_{\text{ext},1}(y_j)$  is high when the values in the observed images are low, causing an increase in the  $U_{\text{ext}}$  value. Conversely, when the values in the observed images are high,  $\phi_{\text{ext},1}(y_j)$  is negative which favors the corresponding position of the associated object.  $\phi_{\text{ext},2}(y_j, y_k)$  penalizes two objects which intersect in an image. The data-driven energy will then have low values for a set of correctly positioned objects which do not have too many similar projections. By minimization, it seems to lead to a desired configuration of objects.

Now, the second term of the energy is presented: the internal energy.

### 2.2.2 Internal energy

In the proposed model, the internal energy function is divided into a sum of two terms and can be written as follows:

$$U_{\text{int}}(y|\theta_{\text{int}}) = U_e(y|\beta) + U_s(y|\gamma_a) \quad (12)$$

The first term  $U_e(y|\beta) = -n(y) \log(\beta)$  is an energy associated with the intensity of the process in terms of the number of objects  $n(y)$  in a configuration. It is defined by the  $\beta$  parameter, which represents the mean number of points by unity of volume in an homogeneous Poisson PP (see section 2.1).

The second term  $U_s(y|\gamma_a) = -n_a(y) \log(\gamma_a)$  allows a Strauss point process which belongs to the family of Markov point processes to be defined [61, 2]. When  $0 \leq \gamma_a < 1$ , this component penalizes the aggregation of objects and to go further in its definition, we need to briefly describe the objects used for tomo-PIV reconstruction. The objects are Gaussian intensity distribution with limited spatial extension defined by a fixed energy percentage (see Eq. 27 & 28 and section 3.1.1 for more details): in 2D, the spatial shape of an object is a circle; in 3D, it is a sphere. In both cases, the spatial extension of the Gaussian intensity distribution is characterized by a radius. If the geometrical mark does not have such a shape, some other choices could be made for the definition of  $U_s$  (see [55] for example).

$n_a(y)$  represents the number of neighbor relationships between objects in the following sense:  $y_i \overset{S}{\sim} y_j$  if  $\|k_i - k_j\|_2 \leq r_i + r_j$  where  $r_i$  and  $r_j$  are the radiuses of  $y_i$  and  $y_j$  respectively. The value of the hyper-parameter  $\gamma_a \in [0, 1]$  controls the outcome of the potential function. If  $\gamma_a = 1$ , the process defined by  $U_{\text{int}}$  behaves as a homogeneous Poisson PP with intensity  $\beta$ . If  $\gamma_a \in ]0, 1[$ , pairs of objects with a distance less than  $r_i + r_j$  are penalized. If  $\gamma_a = 0$ , the process forbids that two objects exist within a distance  $r_i + r_j$ . The process is then said to be hard core.

The proposed model is then parametrized by  $\theta = \theta_{\text{ext}} \cup \theta_{\text{int}}$  with  $\theta_{\text{int}} = \{\beta, \gamma_a\}$ .  $\theta_{\text{ext}}$  is mainly defined by the way objects are projected and discretized on images (see Section 1 & 3.1).

### 2.2.3 OVRMPP - Object Volume Reconstruction based on Marked Point Process

This section describes the MPP dedicated to the reconstruction of 3D objects in Tomo-PIV which represents a particular implementation of the previously proposed MPP. Our aim is to reconstruct a volume of 3D objects based on a set of projection images. Unlike classical tomographic reconstruction methods, the proposed tomographic reconstruction approach, called **OVRMPP**, allows 3D objects that belong to a continuous 3D space to be obtained (see Fig. 2). In view of the elements recalled in section 2.1, points are center positions of 3D objects and marks provide the set of features that characterize each object in the volume: a radius of a sphere and a central intensity (see section 3.1.1). For a configuration,  $y = \{(k_1, m_1), \dots, (k_N, m_{n(y)})\}$ , with  $k_i \in K$  and  $m_i = \{r_i, E_i\} \in M$ ,  $i = 1, \dots, n(y)$ , we have

- $K \subset \mathbb{R}^3$ .
- $M \subset \mathbb{R}^{+2}$  and minimum and maximum values for intensities ( $I_{\text{min}}$  and  $I_{\text{max}}$ ) and radiuses ( $r_{\text{min}}$  and

$r_{\text{max}}$ ) need to be fixed in order to completely define  $M$ .

- The observation data is the set of the  $N$  projection images  $\{I_i, i = 1, \dots, N\}$  with  $I_i = \{o_{i,s}\}_{s \in S_i}$ ,  $S_i$  the set of pixels of  $I_i$ .
- The overlapping of 3D objects must be strongly penalized. Then  $\gamma_a$  (see Section 2.2.2) needs to be taken close to 0 (see Section 3.2 for the values used).

Equation 4 becomes:

$$MSE(y|\{I_i, i = 1, \dots, N\}) = \sum_{i=1}^N \sum_{s \in S_i} (o_{i,s} - p_{i,s})^2 \quad (13)$$

and equations 8, 9 and 10

$$\phi_{\text{ext},1}(y_j) = \sum_{i=1}^N \sum_{s \in S_i, y_j \rightarrow s} p_{y_j \rightarrow s} (p_{y_j \rightarrow s} - 2o_{i,s}) \quad (14)$$

$$U_{\text{ext},2}(y|\theta_{\text{ext}}) = \sum_{i=1}^N \sum_{y_j \overset{i}{\sim} y_k, j < k} \phi_{\text{ext},2}^i(y_j, y_k) \quad (15)$$

where

$$\phi_{\text{ext},2}^i(y_j, y_k) = \sum_{s \in S_i} 2p_{y_j \rightarrow s} p_{y_k \rightarrow s} \quad (16)$$

and  $y_j \overset{i}{\sim} y_k$  means that 2D projections of 3D objects  $y_j$  and  $y_k$  intersect in projection image  $I_i$ . The projection values  $p_{y_j \rightarrow s}$  of object  $y_j$  are computed using the central energy  $E_j$  and equations 25 and 26. The radius that defines the finite extension of  $y_j$  is given in equation 27.

In section 2.4, the 2D case used to obtain a configuration of 2D objects for each projection image will quickly be described.

## 2.3 Simulation of MPP and simulated annealing

### 2.3.1 Metropolis-Hastings-Green algorithm

PP and MPP are classically simulated using the Reversible Jump Markov Chain Monte Carlo method (RJMC-CMC) exploiting a Metropolis-Hastings-Green (MHG) dynamics (or algorithm) [30, 55, 47, 62]. This method allows the simulation of a process with varying sampling spaces. In our case, these sampling spaces are associated with configurations with different numbers of objects. The basic moves of RJMCMC for MPP are the birth and death moves [50, 6, 39]: during these moves, one object is proposed to be either added to or removed from the current configuration.

In addition to these basic moves, supplementary moves can be used: a configuration can be changed by

moving positions of objects or by modifying the mark. To obtain a better position, an object inside the configuration is randomly chosen and new positions are randomly sampled using a uniform probability inside an area around the original position. In case of the use of multiple propositions, the proposed position is the one that gives the minimal value of data-driven energies.

Then, the proposed state for a population  $y$  containing  $d$ -dimensional objects, is  $y' = y \cup \{y_p\}$  for a birth move, where  $y_p$  is a randomly proposed object using a continuous uniform distribution in  $K$  and  $M$ , if no other prior distribution exists. For the death move, the proposed state is  $y' = y \setminus \{y_i\}$ , where  $y$  is uniformly chosen inside  $y$ . For the translation move, the proposed state can then be written as  $y' = y \setminus \{y_i\} \cup \{y_p\}$  where  $y_i, i \in \{1, \dots, n(y)\}$  is a chosen object inside  $y$  and  $k_p$  is randomly chosen near  $k_i$ .

The different propositions are accepted with probability  $\min\{1, \tau_i\}$ ,  $i = B, D$  or  $TR$  (for Birth, Death and Translation), with  $\tau_i$  the MHG acceptance ratio (see Eq. 17, 18 and 19): if  $\tau_i \geq 1$ , the proposition is accepted; otherwise,  $u \sim U_{[0,1]}$  is sampled; if  $u \leq \tau_i$  the proposition is accepted otherwise it is rejected.

Let us denote  $f_b$  the probability of selecting the birth move and  $f_d$  the probability of choosing a death move. In the case of a birth move, the position of the new object  $y$  is chosen randomly following a uniform distribution on the volume  $K$ . Therefore, the MHG ratio can be written as follows when the mark is fixed:

$$\tau_B = \frac{f_d}{f_b} \frac{f(y'|\theta)}{f(y|\theta)} \frac{\nu(K)}{n(y) + 1} \quad (17)$$

and when the mark is not fixed and a uniform law is assumed,  $\tau_B$  is multiplied by  $(r_{max} - r_{min})(I_{max} - I_{min})$  [55].

In the case of a death move, the point to be removed is chosen with a uniform probability on the existing points in the configuration. The following MHG ratio is obtained when the mark is fixed:

$$\tau_D = \frac{f_b}{f_d} \frac{f(y'|\theta)}{f(y|\theta)} \frac{n(y)}{\nu(K)} \quad (18)$$

and when the mark is not fixed and a uniform law is assumed,  $\tau_D$  is divided by  $(r_{max} - r_{min})(I_{max} - I_{min})$ .

In the case of a translation move, The following MHG ratio is obtained:

$$\tau_{TR} = \frac{f(y'|\theta)}{f(y|\theta)} \quad (19)$$

(see Sec. 2.1 for  $\nu(K)$  and  $f(y|\theta)$  is defined in Eq.(1)).

The different propositions are accepted with probability  $\min\{1, \tau_i\}$ ,  $i = B, D$  or  $TR$ . In each case, the ratio  $\frac{f(y'|\theta)}{f(y|\theta)} = \exp\{-\Delta U\}$ , with  $\Delta U = U(y'|\theta) - U(y|\theta)$ ,

only depends on the terms associated to the added, deleted or translated object. For example, in the case of a birth:

$$\Delta U_B = \phi_{d,1}(y_p) + \sum_{y_j \in y, y_p \overset{\sim}{\sim} y_j} \phi_{d,2}(y_p, y_j) - \log\left(\beta \gamma_a^{n_{y_p}}\right) \quad (20)$$

where  $n_{y_p}$  is the number of neighbors of  $y_p$  in  $y$  following the  $\overset{\sim}{\sim}$  neighbor relationship (see Sec. 2.2.2).

### 2.3.2 MAP estimation based on simulated annealing

As previously stated, the MHG algorithm allows configurations of points to be sampled depending on the defined probability density functions. In order to obtain a configuration that minimizes the energy (see Eq. 3), we need to perform a stochastic method of optimization like simulated annealing. This technique is based on the simulation of a non-homogeneous Markov Chain (see [56, 2] for examples with MPP). Simulated annealing needs the definition of a new energy which contains a term  $T$  which can be viewed as a temperature (see Eq. 11 and 12):

$$U_T(y|\theta) = U_e(y|\beta) + \frac{U_{\text{ext}}(y|\theta_{\text{ext}}) + U_s(y|\gamma_a)}{T} \quad (21)$$

and is done by simulating the modified process from a high temperature  $T_0$  to a low temperature  $T_f$ .

$U_e$  is not divided by  $T$  in order to keep constant the prior about the mean number of objects by volume unity during the iterations. Indeed, if  $U_e$  is divided by  $T$ , it means that  $\beta$  becomes  $\beta^{\frac{1}{T}}$  and when  $T$  goes down to zero,  $\beta^{\frac{1}{T}}$  will decrease to zero if  $\beta < 1$  or increase to the infinite if  $\beta > 1$  which is not suitable.

One of the main interests of simulated annealing is that it is supposed to converge whatever the initial configuration which can be the empty configuration for example. But, in our case, we need the convergence of configurations with more than 50,000 3D particles: the dimension of the space to explore is huge. By decreasing the temperature slowly (the optimal decreasing scheme is also intractable), the algorithm will need a huge computation time. Our objective is therefore to obtain an ‘‘accurate’’ configuration in a reasonable time. To this purpose, we propose an initialization method in order to obtain a first configuration of 3D objects.

Let us note that the simulated annealing provides us with a Maximum A Posteriori (MAP) estimation of the 3D objects: the external energy can be used to define the likelihood function and the internal energy the prior about the solution.

The complete algorithm (called **IOD-OVRMPP**) contains the following two steps (see Fig. 3): 1) the IOD method (see next section) that provides a set of 2D detected objects for each projection,  $i = 1, \dots, N$  and the initial 3D object set computed from the 2D object set; 2) OVRMPP method that provides the final 3D object configuration based on a simulated annealing procedure.

#### 2.4 IOD - Initialization method based on Object Detection

In the tomographic reconstruction field where data size is very high, the initialization process is a very important step that can speed up the convergence of the reconstruction methods and enhance the reconstruction quality. To compute a first estimation of the reconstructed volume, we propose an ‘‘Object Oriented’’ method called IOD (Initialization by Object Detection) which was inspired by a 3D position reconstruction technique named ‘‘triangulation’’ often used in the computer vision field. This initialization procedure will be used before the 3D object reconstruction process, whose aim is to obtain a 3D object set with high position accuracy. The operating mode of this 3D object volume initialization method is applied to  $N$  acquired projection images and can be carried out in three main steps (Fig. 3): 1) detection of 2D objects in each projection image; 2) identification of epipolar 2D objects; 3) reconstruction of 3D objects from 2D epipolar objects marks.

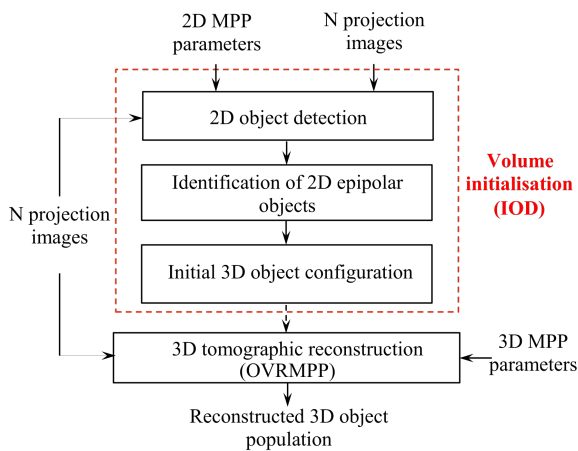


**Fig. 3** Main steps of the proposed method.

##### 2.4.1 1<sup>st</sup> step: 2D object detection

To detect 2D objects in the projection images, a MPP for each projection image is used. In view of the elements recalled in section 2.1, points are now center positions of 2D objects and marks provide the set of features that characterize each object in a projection image: a radius of a circle and a central intensity (see section 3.1.1). For a configuration of 2D objects of the  $i$ th MPP,  $i \in \{1, \dots, N\}$ ,  $y = \{(k_1, m_1), \dots, (k_N, m_{n(y)})\}$ , with  $k_j \in K$  and  $m_j = \{r_j, I_j\} \in M$ ,  $j = 1, \dots, n(y)$ , we have:

- $K \subset \mathbb{R}^2$ .
- $M \subset \mathbb{R}^{+2}$  and minimum and maximum values for intensities and radiuses need to be fixed in order to completely define  $M$ .
- The observation data is a projection image:  $I_i = \{o_{i,s}\}_{s \in S_i}$ ,  $S_i$  the set of pixels of  $I_i$ .
- The overlapping of 2D objects often occurs. Then  $\gamma_a$  (see Section 2.2.2) needs to be taken close to 1 (see Section 3.2 and 3.2 for values used).

For the equations of the MPP, see section 2.2 and equation 25 for the computation of the data-driven energy.

To limit the number of iterations and speed up the convergence of the simulated annealing, we develop a simple initialization procedure, called IRW (Iterative Random Walk), in order to propose a first distribution of 2D objects. To this purpose, one iteration of this procedure is performed in three steps: a simple peak detection is applied to the image which gives a set of detected 2D positions ; each position of this set will be transformed into a 2D object by randomly moving the corresponding position in a short range, in order to enhance its data-driven energy; only a finite number of positions is tested, without the optimization procedure here. A residual image which will be used in the next iteration, is computed between the image used for peak detection and the one generated from the 2D object set. In section 3.2, the number of iterations is fixed equal to two. After this initialization procedure, a simulated annealing optimizes the 2D objects distribution (see Sec. 2.3.2).

##### 2.4.2 2<sup>nd</sup> step: 2D epipolar object identification

Once the detection of 2D objects is completed, a search algorithm to identify 2D epipolar objects is applied. To do that, a geometric correspondence between a point  $\mathbf{X}_0$  in physical space and a point  $\mathbf{x}_0^i$  in the projection image  $I_i$  is determined by the camera optical arrangement. It is described by a projection function  $\psi_i$  defined

as follows:

$$\psi_i(\mathbf{X}_0) = \mathbf{x}_0^i \quad (22)$$

It is considered that the projection of a point in the volume onto a given image is unique. A back-projection function can also be defined; however, for a point  $\mathbf{x}_0^i$  in the image  $I_i$ , there is not one unique corresponding point  $\mathbf{X}_0$  in the volume but a set of points. This set of points, in the volume whose projection is  $\mathbf{x}_0^i$ , is a curve called the line-of-sight  $(LOS)_i(\mathbf{x}_0^i)$ . All the lines-of-sight can be parameterized using the  $Z$  variable [58]. For a given  $Z$ , the back-projection function is defined as follows:

$$\psi_i^{-1}(\mathbf{x}_0^i, Z) = (X, Y, Z) \quad (23)$$

In practice, the projection and back-projection functions are obtained through a rigorous calibration procedure [63]. The camera model used is a pinhole model but other models could be used.

In a perfect case, a set of  $N$  2D objects, which belong to their respective projections, are considered epipolar neighbors if their lines-of-sight intersect in one point. In reality, there is always some noise in the 2D object positions and the lines-of-sight do not intersect. In order to identify epipolar neighbors, the volume where the intersections can be found is decomposed into 3D boxes, placed on a list. For each box, and for each projection, a list of 2D objects whose lines-of-sight cross the box is identified. When in a given box, the list contains one and only one 2D object the procedure is stopped for this box. If one of the 2D object lists is empty, the box is removed from the list. Otherwise, the box is cut into eight boxes which are added to the list. The algorithm goes on like this until it reaches the end of the list. At the end, the box list contains only boxes with epipolar neighbors candidates. Their “intersection” can be defined as the point which minimizes the average distance with all the lines-of-sight. Some of them are false candidates. Two criteria are used to eliminate them:

- their “intersection” must be inside the box
- the intersection error (minimal average distance between the lines-of-sight) must be lower than a given threshold.

If the noise is too strong, wrong epipolar candidates are identified and there is no way of separating false from true candidates. In this case, it is probably not possible to get a good volume reconstruction. And the higher the particle density, the higher the noise influence is. A box list example is shown in figure 4.

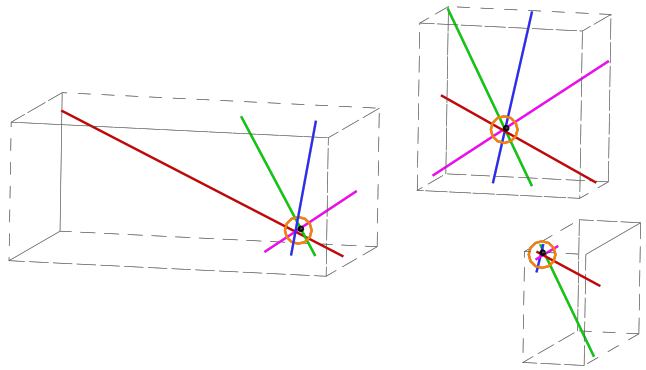


**Fig. 4** Example of a box list. The colored lines represent the lines-of-sight, the black spheres, the theoretical particles and the orange circles, the lines-of-sight “intersection” from noisy data.

#### 2.4.3 3<sup>rd</sup> step: 3D objects initialization

The position of the 3D objects is obtained as the “intersection” of the lines-of-sight of the epipolar neighbors. The mark is chosen such as the average projection size on all images is the same as the average 2D objects size. The link between the 2D and 3D object marks is detailed in section 3.1.1.

In the next section, the application of the proposed “object oriented” approach to Tomo-PIV field is developed.

### 3 Application to fluid mechanics field

In this section, the formalism presented above is applied in the field of fluid mechanics to reconstruct the volumes of 3D particles from a set of projection images. For the sake of brevity, only the experiments made on synthetic data are presented here. We will present some additional results we have obtained studying a turbulent channel flow [25] in a further paper.

#### 3.1 Tomo-PIV technique

As mentioned in the introduction, during the last decade, a lot of developments has been proposed for improving the reconstruction accuracy and for accelerating the calculation. Part of these results has been obtained in the collaborative European framework AFDAR (Advanced Flow Diagnostics for Aeronautical Research [1]). The objective of AFDAR was to focus on new three-dimensional methods based on Particle Image Velocimetry (PIV) for measurement in more industrial applications.

The size of the measurement volume within the laser sheet is fully flexible and can be adapted to measure

small volumes of a few  $mm^3$  as well as large volumes if the light power is sufficient. However, the depth of focus remains a limiting factor. Flow-tracing particles have a real diameter of the order of  $5 - 80 \mu m$  and a spherical shape. Pixel intensities in images constitute spots that represent 2D particles. 2D structures within images are assumed coming from Mie scattering phenomenon [17]. In fact, the diffraction of the laser beams from spherical 3D particles enables its energy to be spread to get 2D projected particles using different viewing angles.

### 3.1.1 Data description and objects of interest

The projection images (Fig.5) used to reconstruct volumes are characterized by their high resolution and high 2D particle density (overlapping of particles phenomenon). The density of particles in the images is measured in particles per pixel (ppp). Intensities of pixels in the images are presented in gray level with particles uniformly distributed on a black noisy background (Fig.5).



**Fig. 5** Real image of 2D particles with  $1200 \times 1600$  pixel size and an estimated seeding density of 0.035 ppp.

The image of a particle in the flow is a spot. The intensity in the image is maximum where the probability of finding the particle position projection is the highest. The spot is characteristic of the uncertainty about the particle position. In real experiments, the distance between the cameras and the measurement volume is quite large, which allows the light beams coming onto the sensors of the cameras to be considered quasi-parallel. Under these assumptions, the model can be simplified and the uncertainty about the position of the 2D particles can be considered isotropic. It is also assumed that it follows a normal distribution.

Volumes to be reconstructed are characterized by their large size and their high density of 3D particles. The density of particles in the discrete volume is measured in particles per voxel (ppv).

The main philosophy of the proposed approach is to reconstruct only objects of interest hence the name “object-oriented” method.

In section 2, we presented MPP based on 2D or 3D objects, each one defined by a mark containing an intensity and a radius. This mark is used to compute data-driven and internal energies (see Sections 2.2.1 and 2.2.2). The radius represents the uncertainty about the position of the object. In the next sections, we provide more details about the marks for 2D and 3D objects and the relationship between them.

### 3.1.2 3D particle

As explained previously, rather than reconstruct the “real” particles, their position and the uncertainty about their position, which is the mark of the objects, are obtained. This approach is linked to our objective to be close to classical methods in order to cross-correlate volumes of particles in order to obtain the most probable displacement.

A 3D particle<sup>1</sup>  $\xi$  can be identified by a 3D continuous position  $\mathbf{X}_0 = (X_0, Y_0, Z_0)^T \in K$  and characterized by its marks  $m_\xi$  containing its maximum value  $E_0$  and its radius  $R$ . These two parameters define completely the uncertainty about the 3D particle position. It is assumed to be an isotropic multivariate Gaussian law and can be computed using the following equation at  $\mathbf{X} = (X, Y, Z)^T \in [-R, R]^3$ :

$$E_\xi(\mathbf{X}) = E_0 \exp \left[ -\frac{(\mathbf{X} - \mathbf{X}_0)^T (\mathbf{X} - \mathbf{X}_0)}{2\sigma_\xi^2} \right] \quad (24)$$

where  $\sigma_\xi$  is the standard deviation of the 3D Gaussian distribution. Outside a sphere of radius  $R$ ,  $E_\xi(\mathbf{X})$  is supposed equal to zero.  $R$  is defined with respect to  $\sigma_\xi$  and  $E_0$  (see Eq. 27) through a coverage factor.  $R$  defines the confidence radius.

The projection of the 3D particle uncertainty is supposed to be conservative, in the sense that the uncertainty about the particle projection position is the projection of the 3D probability distribution on the image. So, for small uncertainties, the 3D isotropic Gaussian distribution modeling the presence probability density is projected onto a 2D isotropic Gaussian distribution, that represents the uncertainty about the projection position.

<sup>1</sup> If the mathematical notations of section 2 which are given for a generic population of objects are considered,  $\xi$  belongs to a population of 3D objects (see Section 2.2.3) and  $\xi = y_i$  for example. Then, we have the following correspondence:  $k_i = \mathbf{X}_0$ ,  $r_i = R$  and  $E_i = E_0$

### 3.1.3 2D particle

Let us define  $\zeta$  a 2D object obtained by the projection of the 3D object  $\xi$ .  $\zeta$  has the position  $\mathbf{x}_0 = (x_0, y_0)^T$  which belongs to a subset of  $\mathbb{R}^2$ . We assume that a 2D particle<sup>2</sup>  $\zeta$  is characterized by a confidence circle of radius  $r$  associated to an isotropic Gaussian intensity distribution with intensity  $I_0$ :  $m_\zeta = (r, I_0)$ . The coverage factor is the same as for the 3D particles. Therefore, the intensity distribution can be computed using the 2D isotropic Gaussian function defined at  $\mathbf{x} = (x, y)^T$  such as  $(x - x_0)^2 + (y - y_0)^2 \leq r^2$  as follows:

$$I_\zeta(\mathbf{x}) = I_0 \exp \left[ - \left( \frac{(x - x_0)^2 + (y - y_0)^2}{2\sigma_\zeta^2} \right) \right] \quad (25)$$

where  $I_0$  is the center intensity and  $\sigma_\zeta$  the standard deviation of the 2D Gaussian probability distribution. Outside the confidence sphere,  $I_\zeta(\mathbf{x})$  is neglected.  $r$  is defined with respect to  $\sigma_\zeta$  and  $I_0$  (see Eq. 28) with the coverage factor.

### 3.1.4 Projection/Back-projection process

Data driven energy used in our reconstruction approach is computed between images and projection of 3D particles. To do this, functions that allow 2D particles to be obtained from a 3D particle and *vice versa* are needed. These functions are called the projection and back-projection process. Projection of a 3D particle on  $N$  projection images gives  $N$  2D epipolar particles. Back-projection of  $N$  epipolar 2D particles gives one 3D particle.

Let  $\xi$  be a 3D particle with an isotropic Gaussian probability distribution, identified by its 3D position  $\mathbf{X}_0$  and characterized by a central intensity  $E_0$  and a confidence radius  $R$ . Let  $\zeta$  be a 2D particle with an isotropic Gaussian probability distribution, identified by its 2D position  $\mathbf{x}_0$  and characterized by a central intensity  $I_0$  and a confidence radius  $r$ . Projection and back-projection processes are performed by finding the correspondence between 3D and 2D marks. To get a 2D particle from a 3D particle in the projection image  $I_i$ , its 2D position  $\mathbf{x}_0^i$  should firstly be computed using equation (22).

Once the central position  $\mathbf{x}_0^i$  of a 2D particle is obtained, its radius and its central probability density can be searched for by evaluating the projection of a 3D particle with isotropic Gaussian distribution profile on

<sup>2</sup> If the mathematical notations of section 2 which are given for a generic population of objects are considered,  $\zeta$  belongs to a population of 2D objects (see Section 2.4.1) and  $\zeta = y_i$  for example. Then, we have the following correspondence:  $k_i = \mathbf{x}_0$ ,  $r_i = r$  and  $E_i = I_0$

a plane. The relation between 2D and 3D central probability density is given by the following equation:

$$I_0 = E_0 \sqrt{2\pi} \sigma_\xi \quad (26)$$

$\sigma_\zeta$  is proportional to  $\sigma_\xi$ . The proportionality constant depends only on the camera model. The standard deviation  $\sigma_\xi$  is used to compute a discrete map of a 3D particle to discretize the volume of particles after reconstruction. The discrete maps are generated so that the probability of the particle of being inside a sphere of radius  $R$  reaches a confidence level  $\delta$ . The radius is given by equation (27) where  $k_{3D}(\delta)$  is the 3D coverage factor:

$$R = k_{3D}(\delta)\sigma_\xi \quad (27)$$

For example, for  $\delta = 90\%$  we have  $k_{3D}(\delta) = 2.55$ . After the completion of the projection process of a 3D particle, a discrete map is also computed for each 2D particle using the same confidence level  $\delta$  as for an isotropic Gaussian distribution. Discrete maps related to 2D particles are used to compute the data-driven energy (see Eq. 8 and 10). To get the discrete map, the standard deviation  $\sigma_\zeta$  of the Gaussian should firstly be computed. In the same way as above,  $\sigma_\zeta$  is given by:

$$r = k_{2D}(\delta)\sigma_\zeta \quad (28)$$

where  $k_{2D}(\delta)$  is the 2D coverage factor.

To study the performance of the proposed approach, tests were conducted on simulated data (results on real data are given in [11]). Our approach was adapted to the measurement of flows and called IOD-PVRMPP (Iterative Object Detection - Particle Volume Reconstruction based on Marked Point Process) since it was used to reconstruct the population of 3D particles. A comparison between IOD, IOD-PVRMPP and MinLOS-MART which is a reference algebraic reconstruction method in Tomo-PIV will be presented in the following sections. The comparison is performed using several evaluation criteria.

## 3.2 Results on synthetic data

A set of synthetic volumes with associated projected images are generated using an image generator developed in C++ using the SLIP library [60] and inspired by Lecordier and Westerweel [37]. The synthetic volume size is  $500 \times 500 \times 150$ . Four projections of size  $500 \times 500$ , with image seeding density varying from 0.0004 to 0.2 ppp (Fig. 6), are then computed knowing that 0.05 ppp is the required seeding density level for Tomo-PIV field [26]. 2D and 3D particles are characterized by marks as described in section 3.1 and [9, 10]. The number of 3D

particles  $N_p$  in synthetic volumes, generated for each seeding density level, vary from 100 up to 50000 particles.

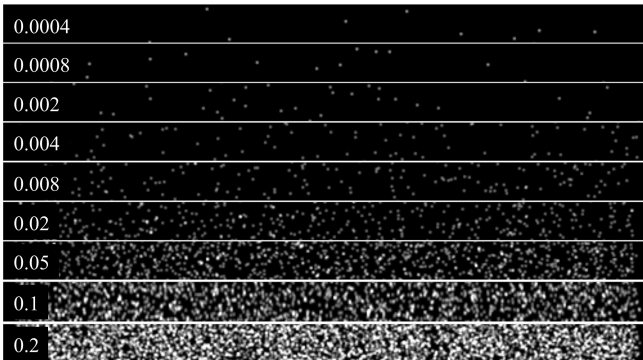


**Fig. 6** Bands extracted from simulated images with different concentrations of particles. The density of particles of each band is indicated in particles per pixel (ppp).

For this experimental study, the intensity center and the radius of all particles are fixed: the diameter size is 5 voxels for 3D particles and 3 pixels for 2D particles; the distribution of intensities around all center positions of particles is modeled as a multivariate isotropic Gaussian density. The calibration model is a pinhole model, without distortions. The acquisition system is simulated with 4 cameras ( $N = 4$ ): two cameras on one side with a  $30^\circ$  viewing angle; two other cameras on the other side of the volume, on the same plane (Fig. 7).

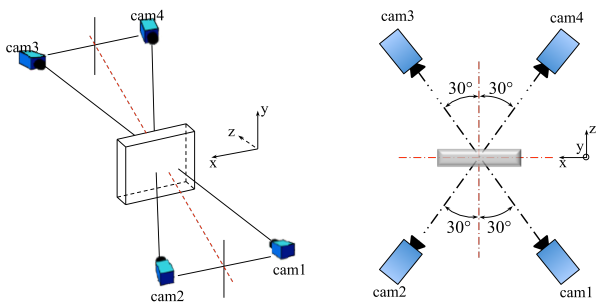


**Fig. 7** Camera positions for the simulated cases.

For IOD and PVRMPP, a set of parameters is chosen for each seeding density in order to get a good reconstruction of 3D particle volumes (see tables 1 and 2). These parameter choices were adopted after several simulations, trying to find the best trade-off between reconstruction quality, ghost particle rate and computation time. In tables 1 and 2,  $f_{tr}$  corresponds to the probability of selecting the translation move. Birth and death moves are chosen with the probability  $1 - f_{tr}$ , and, in a second random selection, with the probabilities  $f_b$

and  $f_d$  respectively ( $f_d = 1 - f_b$ ).  $\gamma_a$  is fixed to 0.05 (see Section 2.2.3). The simulated annealing algorithm is configured with an initial temperature  $T_0$  and with a fixed final temperature  $T_f$  equal to 0.02. A classical cooling scheme is chosen:  $T_t = T_0 q^t$  with  $t$  the current iteration,  $q = \left(\frac{T_f}{T_0}\right)^{\frac{1}{N_{it}}}$  the parameter of the cooling scheme and  $N_{it}$  the number of iterations. Each iteration consists in one proposed “Birth”/“Death”/“Translation” move of MHG algorithm, which may be accepted or not (see Section 2.3).

PPP	$N_p$	$\gamma_a$	$\beta$	$f_b$	$f_{tr}$	$N_{it}$	$T_0$
0,0004	100	0,6	0,0004	0,5	0,5	$1.5 \cdot 10^4$	0,025
0,0008	200	0,6	0,0008	0,5	0,5	$1.8 \cdot 10^4$	0,025
0,0020	500	0,9	0,002	0,5	0,5	$4 \cdot 10^4$	0,025
0,0040	1000	0,9	0,004	0,5	0,5	$1 \cdot 10^5$	0,025
0,0080	2000	0,9	0,008	0,5	0,5	$1.5 \cdot 10^5$	0,025
0,0200	5000	0,9	0,02	0,6	0,5	$5.5 \cdot 10^5$	0,025
0,0500	12500	0,9	0,05	0,75	0,4	$5 \cdot 10^6$	0,035
0,1000	25000	0,95	0,1	0,75	0,4	$1 \cdot 10^7$	0,035
0,2000	50000	0,95	0,2	0,75	0,4	$1.5 \cdot 10^7$	0,035

**Table 1** Sets of parameters used for the IOD method applied to synthetic data.

PPP	$N_p$	$\beta$	$f_b$	$f_{tr}$	$N_{it}$	$T_0$
0.0004	100	$2.66 \cdot 10^{-6}$	0.50	0.50	$1.5 \cdot 10^4$	0.025
0.0008	200	$5.33 \cdot 10^{-6}$	0.50	0.50	$1.8 \cdot 10^4$	0.025
0.0020	500	$1.33 \cdot 10^{-5}$	0.50	0.50	$2.4 \cdot 10^4$	0.035
0.0040	1000	$2.66 \cdot 10^{-5}$	0.50	0.50	$5 \cdot 10^4$	0.045
0.0080	2000	$5.33 \cdot 10^{-5}$	0.50	0.50	$1.3 \cdot 10^5$	0.045
0.0200	5000	$1.33 \cdot 10^{-4}$	0.60	0.50	$5.5 \cdot 10^5$	0.048
0.0500	12500	$3.33 \cdot 10^{-4}$	0.75	0.40	$8.1 \cdot 10^6$	0.850
0.1000	25000	$6.66 \cdot 10^{-4}$	0.75	0.40	$2.5 \cdot 10^7$	0.850
0.2000	50000	$1.33 \cdot 10^{-3}$	0.75	0.40	$3.2 \cdot 10^7$	0.850

**Table 2** Sets of parameters used for the PVRMPP reconstruction method applied to synthetic data.

To evaluate the performances of IOD-PVRMPP method, some quantitative measurements are computed and compared to those obtained with MinLOS-MART [58], with a fixed number of iterations equal to 5, which can be considered as a reference algorithm within our application. The results of IOD method are also given to show the improvement obtained between initial and final populations of points. All measures are computed by taking 10 reconstructed samples (volumes) for the IOD-PVRMPP method given the random nature of the algorithm.

First, two examples of evolutions of the cumulative mean of the number of 3D objects ( $N_p$ ) in the population during PVRMPP are presented, with an initial population obtained with IOD (Fig. 8). These curves are truncated showing about the first half of the iterations. Two main types of evolution are observed: for ppp lower than 0.05,  $N_p$  globally increases before reaching a value close to the true number of particles. For ppp higher than 0.1, IOD provides a population with a lot of generated ghost 3D objects. Then, many 3D objects are deleted at high temperature (during the first itera-

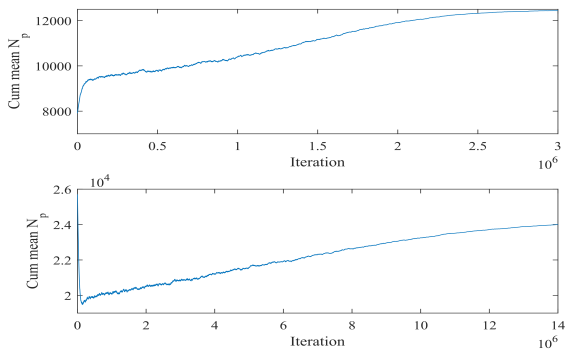


**Fig. 8** Cumulative means of the number of particles inside the volume during two PVRMPP runs. top: ppp = 0.05; true number = 12500; initial number after IOD = 7925; estimated number = 12491. bottom: ppp = 0.1; true number = 25000; initial number after IOD = 25704; estimated number = 24448.

tions). After this phase,  $N_p$  increases and converges to the true number of particles.

To evaluate the reconstruction quality, the cross-correlations ( $Q_v$ ) between the reconstructed volumes and the reference volumes are computed:

$$Q_v = \frac{\sum_{i=0}^{N_v} (V_r(i) - \bar{V}_r) (V_{ref}(i) - \bar{V}_{ref})}{\sqrt{(V_r - \bar{V}_r)^2} \sqrt{(V_{ref} - \bar{V}_{ref})^2}} \quad (29)$$

with  $N_v$  the number of voxels,  $V_r$  the reconstructed volume and  $V_{ref}$  the reference volume. Figure 9 shows that IOD-PVRMPP provides better results than MinLOS-MART for seeding densities up to 0.1 ppp. The reconstruction quality of the IOD-PVRMPP method decreases when the overlapping between 2D particles in images increases.

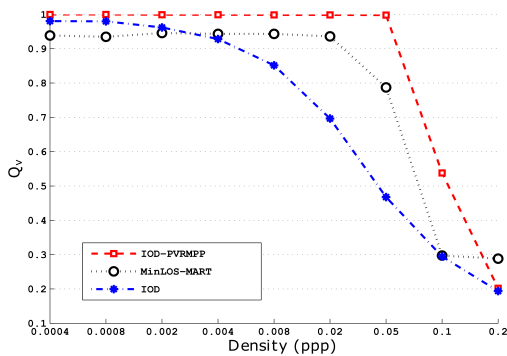


**Fig. 9** Evolution of the volume reconstruction quality  $Q_v$  as a function of the density of particles.

To evaluate the accuracy of the IOD-PVRMPP method, error positions ( $E_v$ ) between 3D particle positions in reconstructed volumes and the reference volumes are computed. Results show a very high level of accuracy with error average varying between 0.01 to 0.043 voxels for seeding densities up to 0.05 ppp (Fig.10). Curves in (Fig.11) show very low rates of detected ghost particles with IOD-PVRMPP which vary between 0 and

0.098% for seeding density up to 0.05 ppp against 2.92 to 47.74% with MinLOS-MART.

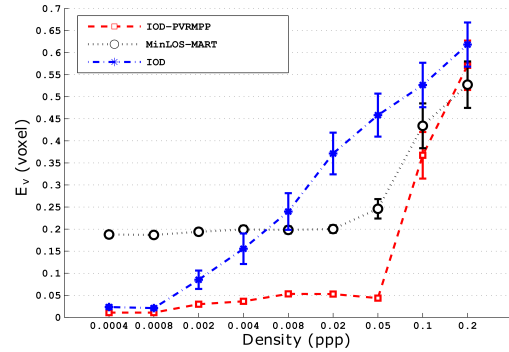


**Fig. 10** Evolution of the mean error position inside the volume as a function of the density of particles.

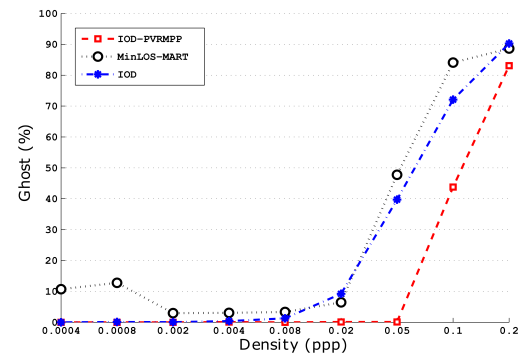


**Fig. 11** Evolution of percentage of number of ghost particles as a function of the density of particles

Some samples of projections after volume reconstruction are presented in figure (12) in order to provide some qualitative results.

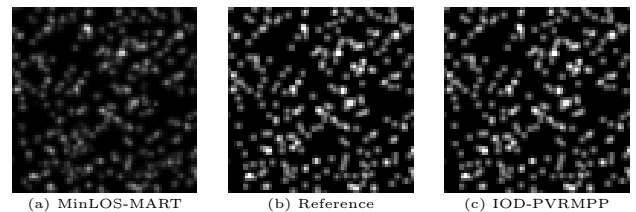


**Fig. 12** Comparison of the projections (region with size  $64 \times 64$ ) of a reconstructed volume of particles onto a camera for (a) MinLOS-MART, (b) Reference (c) IOD-PVRMPP for a 0.05 ppp seeding density level. The images are originally encoded with 16 bits unsigned integers and differences between the images (b) and (c) are difficult to observe.

The results obtained above can be visually observed in a slice of the reconstructed volumes. In order to view 3D particles inside volumes and visually compare the results, Y-axis slices of volumes reconstructed with 0.05 ppp image density using MinLOS-MART and IOD-PVRMPP methods are extracted. A slice of the reconstructed volume using MinLOS-MART method shows several particle position errors like ghost 3D particles

(red circles) and false-negative 3D particles (blue circles) as opposed to the IOD-PVRMPP reconstructed slice that is very close to the reference slice (Fig. 13).

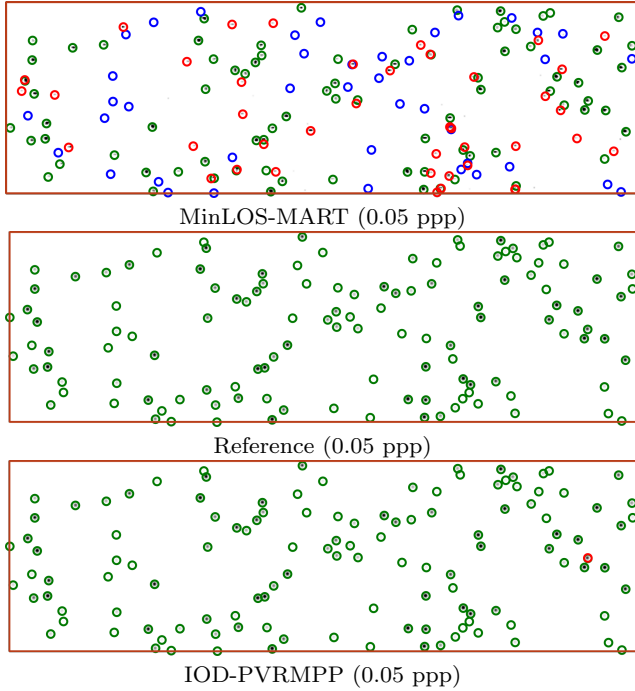


**Fig. 13** Y-axis slices issued from volumes reconstructed with MinLOS-MART and IOD-PVRMPP methods using 0.05 *ppp* image density. Green circles represent true particles, red circles represent ghost particles and blue circles represent non-reconstructed particles (false-negative particles). The magenta color is derived from the superposition of red and blue circles.

The features of 3D particles located in the reconstructed volumes have a direct influence on the quality of the reconstruction and the cross-correlation to generate 3D velocity field. In order to see the influence of the reconstruction quality on the quality of velocity fields without considering correlation algorithm errors, the measurement criterion  $Q_c$  named correlation quality is used [58]. This criterion is defined as follows:

$$Q_c = \sqrt{\frac{\sum_{i=0}^{N_{vf}} \|u_{ref}(i) - u_a(i)\|^2}{\sum_i^{N_{vf}} \|u_r(i) - u_a(i)\|^2}} \quad (30)$$

where  $N_{vf}$  is the number of positions where the velocity field is computed,  $u_{ref}$  the velocity field generated from the reference volumes (synthetic),  $u_a$  the analytical velocity field, and  $u_r$  the velocity field computed from the reconstructed volumes.

To do this, data with 0.05 *ppp* level density is used. Particles belonging to each pair of successive volumes follow a simulated sinusoidal movement. The 3D coordinates  $(x_d, y_d, z_d)$  of a particle after displacement depend on its initial coordinates  $(x, y, z)$  and are calculated using the equations  $x_d = A \sin(\omega z) + C \cos(\omega y)$ ,  $y_d =$

$B \sin(\omega x) + A \cos(\omega z)$  et  $z_d = C \sin(\omega y) + B \cos(\omega x)$  with  $A = \sqrt{3}$ ,  $B = \sqrt{2}$ ,  $C = 1$  and  $\omega = 1/20$ . The coordinates  $(U, V, W)$  at each position of the velocity field depend on the coordinates of the particles after the motion and are calculated as follows:

$$(U, V, W) = \left( \frac{x_d - x}{\Delta t}, \frac{y_d - y}{\Delta t}, \frac{z_d - z}{\Delta t} \right) \quad (31)$$

with  $\Delta t$  the temporal step fixed at one voxel.

The IOD-PVRMPP method provides a velocity field of quality equal to  $Q_c = 0.99$  compared to  $Q_c = 0.89$  for the MinLOS-MART method. To generate velocity fields, a multi-pass cross-correlation algorithm developed in the context of the French VIVE3D project using the SLIP library is used [60]. The cross-correlation results were obtained using search windows with dimension  $32 \times 32 \times 32$  voxels and an overlap of 75%. Vector fields were validated by a  $5 \times 5 \times 5$  voxel local median filter size. False vectors were replaced by the median value.

In order to assess the results obtained by calculating the quality correlation criteria  $Q_c$ ,  $L_2$  distance map  $D$  between the velocity field and the reference one were computed for MinLOS-MART and IOD-PVRMPP. The results are shown on Fig. 14. They confirm the numerical result obtained with the  $Q_c$  criterion.

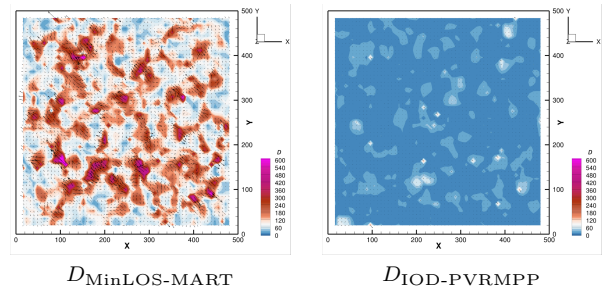


**Fig. 14**  $L_2$  Distance map  $D$  (mm/s) on  $XY$  plane, to assess IOD-PVRMPP and MinLOS-MART methods for 0.05 *ppp* level density particles.

Representation of particles via marks takes up very little space compared to representation inside a 3D array volume. Indeed, if, as in our implantation only six parameter values are associated to a particle, the memory size of a set of marks characterizing a 3D particle is equal to 496 bytes. Consequently populations of particles varying from 100 to 50000 elements used in our experiments need only 0.05 to 24.80 MB storage. In comparison, for the MinLOS-MART method, the required memory is linked to the dimensions  $500 \times 500 \times 150$  voxels of the discrete volume which corresponds to 286 MB storage. Gain in memory storage for IOD-PVRMPP increases as the size of the volume increases.

## 4 Conclusion

In this paper, we have presented a new approach called IOD-OVRMPP for the reconstruction of a population of 3D objects, including an initialization procedure, using the Marked Point Process framework. Rather than a “voxel-oriented” approach, our work uses an “object-oriented” approach. It allows the problem to be solved in a parsimonious way and provides a MAP estimation: the reconstruction of a 3D object set is obtained by minimizing an energy function thanks to a simulated annealing based on an MHG algorithm. To speed up the convergence of the simulated annealing, an initialization method has been developed. It provides the initial distribution of 3D objects based on the detection of 2D objects located in projection images. The IOD-OVRMPP approach works in a continuous space where 2D and 3D objects are identified by real positions. This mathematical formalism is very suitable for the reconstruction of sparse solutions since it reconstructs only objects, unlike voxel-oriented methods of tomographic reconstruction which use all the voxels to finally provide a discrete volume.

The proposed approach is applied to the Tomo-PIV field to reconstruct volumes of 3D particles. The method is validated on synthetic data. Results show the relevance of the proposed data-driven energy for the reconstruction of a volume of 3D particles. The method is compared to an algebraic reconstruction method called MinLOS-MART. The IOD-PVRMPP method improves the quality of reconstruction even for high particle densities (up to and even more than 0.05 ppp). The position error and ghost particle rate are greatly reduced with IOD-PVRMPP: 3D position error is equal to 0.043 voxels, compared to 0.25 voxels with MinLOS-MART for 0.05 ppp particle density. For the same particle density, the number of ghost particles is approximately 0.1%, against 47.7% with MinLOS-MART. IOD-PVRMPP also provides a better memory usage: the amount of RAM used to run the method is less compared to classical volumetric memory usage.

Future work will include the optimization of the IOD-PVRMPP algorithm to speed up the reconstruction as well as a full comparison with the Shake the Box method [52] or the SMTE method for time resolved acquisitions [41]. Then the IOD-PVRMPP method will be improved in order to handle particle blurring due to a small depth of field and astigmatism due to imaging optics. This approach will also be tested in other domains such as digital holography for example, to see its capacity to reconstruct 3D object volumes using different data.

## Appendix A Data Driven Energy calculation details

If the square of equation (4) is developed, the following result is obtained:

$$MSE(y|o) = \sum_{s \in S} o_s^2 + p_s^2 - 2o_s p_s \quad (32)$$

The first term of the addition in equation (32) is constant. The data-driven energy defining the likelihood between the projection of a configuration  $y$  and the observed data  $o = \{o_s\}_{\{s \in S\}}$  can be written:

$$U_{\text{ext}}(y) = \sum_{s \in S} p_s^2 - 2o_s p_s \quad (33)$$

$U_{\text{ext}}$  defines the quality of a configuration compared to the data: the closer the projection of a population of objects is to the reference image, the lower its energy value. We show below that this energy can be written as a sum of first-order and second-order neighborhood energy terms.

Using equation (5), equation (33) can be written:

$$U_{\text{ext}}(y) = \sum_{s \in S} \left[ \left( \sum_{y_j, y_j \rightarrow s} p_{y_j \rightarrow s} \right)^2 - 2 o_s \left( \sum_{y_j, y_j \rightarrow s} p_{y_j \rightarrow s} \right) \right] \quad (34)$$

$$U_{\text{ext}}(y) = \sum_{s \in S} \left[ \left( \sum_{y_j, y_j \rightarrow s} p_{y_j \rightarrow s}^2 + 2 \sum_{\substack{y_j, y_k, j < k \\ y_j \rightarrow s, y_k \rightarrow s}} p_{y_j \rightarrow s} p_{y_k \rightarrow s} \right) - 2 o_s \left( \sum_{y_j, y_j \rightarrow s} p_{y_j \rightarrow s} \right) \right] \quad (35)$$

$$U_{\text{ext}}(y) = \sum_{s \in S} \sum_{y_j, y_j \rightarrow s} p_{y_j \rightarrow s} (p_{y_j \rightarrow s} - 2 o_s) + \sum_{s \in S} 2 \sum_{\substack{y_j, y_k, j < k \\ y_j \rightarrow s, y_k \rightarrow s}} p_{y_j \rightarrow s} p_{y_k \rightarrow s} \quad (36)$$

$$U_{\text{ext}}(y) = \underbrace{\sum_{y_j \in y} \sum_{\substack{s \in S \\ y_j \rightarrow s}} p_{y_j \rightarrow s} (p_{y_j \rightarrow s} - 2 o_s)}_{\text{first-order term}} + \underbrace{\sum_{\substack{y_j, y_k, j < k \\ y_j \sim y_k}} \sum_{\substack{s \in S \\ y_j \rightarrow s \ \& \ y_k \rightarrow s}} 2 p_{y_j \rightarrow s} p_{y_k \rightarrow s}}_{\text{second-order term}} \quad (37)$$

**Acknowledgements** The current work has been conducted as part of the AFDAR project, Advanced Flow Diagnostics for Aeronautical research, funded by the European Commission program FP7, Grant No. 265695 and also the FEDER project No. 34754.

## References

1. AFDAR: Advanced flow diagnostics for aeronautical research. URL [www.afdar.eu](http://www.afdar.eu)
2. Alata, O., Burg, S., Dupas, A.: Grouping/degrouper point process, a point process driven by geometrical and topological properties of a partition in regions. *Computer Vision and Image Understanding* **115**, 1324–1339 (2011)
3. Andersen, A.H., Kak, A.C.: Simultaneous algebraic reconstruction technique (SART): a superior implementation of the ART algorithms. *Ultrasonic imaging* **6**(1), 81–94 (1984)
4. Atkinson, C.H., Soria, J.: An efficient simultaneous reconstruction technique for tomographic particle image velocimetry. *Experiments in Fluids* **47**(4-5), 553–568 (2009). DOI 10.1007/s00348-009-0728-0
5. Azencott, R.: *Simulated annealing: Parallelization techniques*. Springer-Verlag, NY (1992)
6. Baddeley, A.J., Lieshout, M.N.M.V.: Stochastic geometry models in high-level vision. *Journal of Applied Statistics* **20**(5-6), 231–256 (1993). DOI 10.1080/02664769300000065
7. Belden, J., Truscott, T.T., Axiak, M.C., Techet, A.H.: Three-dimensional synthetic aperture particle image velocimetry. *Measurement Science and Technology* **21**(12), 125,403 (2010)
8. Ben-Salah, R.: *Élaboration d'une méthode tomographique de reconstruction 3D en vélocimétrie par image de particules basée sur les processus ponctuels marqués*. Ph.D. thesis, Université de Poitiers, Faculté des Sciences Fondamentales et Appliquées, Poitiers (2015)
9. Ben-Salah, R., Alata, O., Thomas, L., Tremblais, B., David, L.: 3d particle volume tomographic reconstruction based on marked point process: Application to tomo-piv in fluid mechanics. In: *IEEE International Conference on Acoustics, Speech and Signal Processing (ICASSP)*, pp. 8153–8157. IEEE (2014)
10. Ben-Salah, R., Alata, O., Tremblais, B., Thomas, L., David, L.: Particle volume reconstruction based on a marked point process and application to tomo-piv. In: *European Signal Processing Conference (EUSIPCO 2015)*. Nice (France) (2015)
11. Ben-Salah, R., Thomas, L., Tremblais, B., Alata, O., David, L.: Reconstruction de volumes de particules par processus ponctuels marqués. In: *CFTL2016, 15ème Congrès Francophone de Technique Laser pour la Mécanique des Fluides*. Toulouse, France (2016). URL <https://hal.archives-ouvertes.fr/hal-01368625>
12. Benson, T.M., Gregor, J.: Modified simultaneous iterative reconstruction technique for faster parallel computation. In: *Nuclear Science Symposium Conference Record, IEEE*, vol. 5, pp. 2715–2718. IEEE (2005)
13. Byrne, C.: Block-iterative algorithms. *International Transactions in Operational Research* **16**(4), 427–463 (2009). DOI 10.1111/j.1475-3995.2008.00683.x
14. Censor, Y.: Finite series-expansion reconstruction methods. *Proceedings of the IEEE* **71**(3), 409–419 (1983)
15. Champagnat, F., Cornic, P., Cheminet, A., Leclaire, B., Le-Besnerais, G., Plyer, A.: Tomographic piv: particles versus blobs. *Measurement Science and Technology* **25**(8), 084,002 (2014)
16. Chatelain, F., Costard, A., Michel, O.J.J.: A bayesian marked point process for object detection. application to muse hyperspectral data. In: *IEEE ICASSP 2011*, pp. 3628–3631 (2011). DOI 10.1109/ICASSP.2011.5947136
17. Chýlek, P., Zhan, J.: Absorption and scattering of light by small particles: the interference structure. *Appl. Opt.* **29**(28), 3984–3984 (1990). DOI 10.1364/AO.29.003984
18. Daley, D.J., Vere-Jones, D.: *An Introduction to the Theory of Point Processes: Volume I: Elementary Theory and Methods*, Second Edition, vol. 1, 2nd edn. Springer edn. Springer, New York (2003)
19. Darroch, J.N., Ratcliff, D.: Generalized iterative scaling for log-linear models. *The annals of mathematical statistics* **43**(3), 1470–1480 (1972)
20. Dean, V.: Limited-data computed tomography algorithms for the physical sciences. *Appl. Opt.* **32**(20), 3736–3754 (1993). DOI 10.1364/AO.32.003736
21. Dempster, A.P., Laird, N.M., Rubin, D.B.: Maximum likelihood from incomplete data via the EM algorithms. *Journal of the Royal Statistical Society. Series B (Methodological)* **39**(1), 1–38 (1977)
22. Descamps, S., Descombes, X., Bechet, A., Zerubia, J.: Automatic flamingo detection using a multiple birth and death process. In: *IEEE ICASSP 2008*, pp. 1113–1116 (2008). DOI 10.1109/ICASSP.2008.4517809
23. Discetti, S., Astarita, T.: Fast multi-resolution 3D PIV with direct correlations and sparse arrays. In: *Forum on recent developments in Volume Reconstruction techniques applied to 3D fluid and solid mechanics*. Poitiers, France (2011)
24. Donoho, D.L., Tanner, J.: Counting the faces of randomly-projected hypercubes and orthants, with applications. *Discrete & computational geometry* **43**(3), 522–541 (2010)
25. Earl, T., Ben-Salah, R., Thomas, L., Tremblais, B., Cochard, S., David, L.: Volumetric measurements by tomographic piv of an open channel flow behind a turbulent grid. In: *18th Australasian Fluid Mechanics Conference*, pp. 978–1 (2013)
26. Elsinga, G.E., Scarano, F., Wieneke, B.: Tomographic particle image velocimetry. *Exp Fluids* **41**, 933–947 (2006)
27. Gamboa, F.: *Méthode du maximum d'entropie sur la moyenne et applications*. Ph.D. thesis, Université de Paris-Sud, Orsay (1989)
28. Geman, S., Geman, D.: Stochastic relaxation: gibbs distributions and the bayesian restoration of images. *IEEE Trans. on PAMI* **9**, 721–741 (1984)
29. Gordon, R., Bender, R., Herman, G.T.: Algebraic reconstruction techniques (ART) for three-dimensional electron microscopy and X-ray photography. *Journal of Theoretical Biology* **29**(3), 471–481 (1970). DOI [http://dx.doi.org/10.1016/0022-5193\(70\)90109-8](http://dx.doi.org/10.1016/0022-5193(70)90109-8)
30. Green, P.J.: Reversible jump markov chain monte carlo computation and bayesian model determination. *Biometrika* **82**(4), 711–732 (1995). DOI 10.1093/biomet/82.4.711
31. Hadamard, J.: *Le probleme de Cauchy et les équations aux dérivées partielles linéaires hyperboliques*, vol. 193. Paris (1932)
32. Herman, G.T., Arnold, L.: Iterative reconstruction algorithms. *Comput. Biol. MA.* **6**(4), 273–294 (1976)

33. Herzet, C., Drémeau, A.: Bayesian pursuit algorithms. In: Proc. European Signal Processing Conference (EU-SIPCO). Aalborg, Denmark (2010)
34. Hudson, H.M., Larkin, R.S.: Accelerated image reconstruction using ordered subsets of projection data. *Medical Imaging, IEEE Transactions on* **13**(4), 601–609 (1994)
35. Kaczmarz, S.: Angenäherte auflösung von systemen linearer gleichungen. *Bulletin International de l'Académie Polonaise des Sciences et des Lettres* **35**, 355–357 (1937)
36. Lascaux, P., Théodor, R.: Analyse numérique matricielle appliquée à l'art de l'ingénieur, tome 2 : Méthodes itératives, vol. 2. Masson Paris, France (2004)
37. Lecordier, B., Westerweel, J.: The EUROPIV Synthetic Image Generator (S.I.G.). In: J.K.E. M. Stanislas J. Westerweel (ed.) Proceedings of the EUROPIV 2 Workshop on Particle Image Velocimetry. Springer Verlag (2004)
38. Lewitt, R.M.: Reconstruction algorithms: transform methods. *Proceedings of the IEEE* **71**(3), 390–408 (1983)
39. Lieshout, M.N.M.V.: Markov point processes and their applications. Imperial College Press/World Scientific Publishing, (2000)
40. Lu, W., Yin, F.F.: Adaptive algebraic reconstruction technique. *Medical physics* **31**(12), 3222–3230 (2004)
41. Lynch, K.P., Scarano, F.: An efficient and accurate approach to MTE-MART for time-resolved tomographic PIV. *Experiments in Fluids* **56**(3), 1–16 (2015). DOI 10.1007/s00348-015-1934-6
42. Maas, H.G., Westfeld, P., Putze, T., Bøtkjær, N., Kitzhofer, J., Brücker, C.: Photogrammetric techniques in multi-camera tomographic piv. In: Proceedings of the 8th International Symposium on Particle Image Velocimetry, pp. 25–28 (2009)
43. Mallet, C., Lafarge, F., Roux, M.J., Soergel, U., Bretar, F., Heipke, C.: A Marked Point Process for Modeling Lidar Waveforms. *IEEE Transactions on Image Processing* **19**(12), 3204–3221 (2010). DOI 10.1109/TIP.2010.2052825
44. Minerbo, G.: MENT: A maximum entropy algorithm for reconstructing a source from projection data. *Computer Graphics and Image Processing* **10**(1), 48–68 (1979)
45. Ortner, M., Descombes, X., Zerubia, J.: Building outline extraction from digital elevation models using marked point processes. *Int. J. Computer Vision* **72**(2), 107–132 (2007). DOI 10.1007/s11263-005-5033-7
46. Perrin, G., Descombes, X., Zerubia, J.: Adaptive simulated annealing for energy minimization problem in a marked point process application. In: Energy Minimization Methods in Computer Vision and Pattern Recognition, *LNCS*, vol. 3757, pp. 3–17. Springer Berlin Heidelberg (2005). DOI 10.1007/11585978\_1
47. Perrin, G., Descombes, X., Zerubia, J.: 2d and 3d vegetation resource parameters assessment using marked point processes. In: Pattern Recognition, 2006. ICPR 2006. 18th International Conference on, vol. 1, pp. 1–4 (2006). DOI 10.1109/ICPR.2006.20
48. Petra, S., Schröder, A., Schnörr, C.: 3D tomography from few projections in experimental fluid dynamics. In: W. Nitsche, C. Dobriloff (eds.) *Imaging Measurement Methods for Flow Analysis, Notes on Numerical Fluid Mechanics and Multidisciplinary Design*, vol. 106, pp. 63–72. Springer Berlin Heidelberg (2009). DOI 10.1007/978-3-642-01106-1\_7
49. Peyrin, F., Garnero, L., Magnin, I.: Introduction à l'imagerie tomographique 2D et 3D reposant sur une propagation en ligne droite. cas de la tomographie par rayon X, par émission et par ultrasons. *Traitement du signal* **13**(4), 381–413 (1996)
50. Preston, C.J.: Spatial birth-and-death processes. *Bulletin of the International Statistical Institute* **46**, 371–391 (1977)
51. Rietch, E.: The maximum entropy approach to inverse problems. *J. Geophys* **42**, 489–506 (1977)
52. Schanz, D., Schröder, A., Gesemann, S., Michaelis, D., Wieneke, B.: Shake The Box: A highly efficient and accurate Tomographic Particle Tracking Velocimetry (TOMO-PTV) method using prediction of particle positions (2013)
53. Schmidlin, P.: Iterative separation of sections in tomographic scintigrams. *Nuclear-Medizin* **11**(1), 1 (1972)
54. Shepp, L.A., Vardi, Y.: Maximum likelihood reconstruction for emission tomography. *Medical Imaging, IEEE Transactions on* **1**(2), 113–122 (1982)
55. Stoica, R., Descombes, X., Zerubia, J.: A gibbs point process for road extraction from remotely sensed images. *Int. J. Computer Vision* **57**(2), 121–136 (2004). DOI 10.1023/B:VISI.0000013086.45688.5d
56. Stoica, R., Martinez, V., Mateu, J., Saar, E.: Detection of cosmic filaments using the candy model. *Astron.Astrophys* **434**, 423–432 (2005). DOI 10.1051/0004-6361:20042409
57. Sun, K., Sang, N., Zhang, T.: Marked point process for vascular tree extraction on angiogram. In: Energy Minimization Methods in Computer Vision and Pattern Recognition, *LNCS*, vol. 4679, pp. 467–478. Springer Berlin Heidelberg (2007). DOI 10.1007/978-3-540-74198-5\_36
58. Thomas, L., Tremblais, B., David, L.: Optimization of the volume reconstruction for classical tomo-piv algorithms (mart, bimart and smart): synthetic and experimental studies. *Measurement Science and Technology* **25**(3), 035,303 (2014)
59. Tournaire, O., Paparoditis, N., Lafarge, F.: Rectangular road marking detection with marked point processes. *Proc. conference on Photogrammetric Image Analysis* **36**(3/W49A), 149–154 (2007)
60. Tremblais, B., David, L., Arrivault, D., Dombre, J., Chatellier, L., Thomas, L.: Slip : Simple Library for Image Processing (version 1.0). <http://sliplib.free.fr> (2010). URL <http://sliplib.free.fr>
61. Van-Lieshout, M.N.M.: Markov point processes and their applications. Imperial College Press/World Scientific Publishing, (2000)
62. Weina, G., Collins, R.: Marked point processes for crowd counting. In: Computer Vision and Pattern Recognition, 2009. CVPR 2009. IEEE Conference on, pp. 2913–2920 (2009). DOI 10.1109/CVPR.2009.5206621
63. Wieneke, B.: Volume self-calibration for 3D particle image velocimetry. *Experiments in Fluids* **45**(4), 549–556 (2008)
64. Wieneke, B.: Iterative reconstruction of volumetric particle distribution. *Measurement Science and Technology* **24**(2), 024,008 (2013)
65. Worth, N.A., Nickels, T.B.: Acceleration of tomo-piv by estimating the initial volume intensity distribution. *Experiments in Fluids* **45**(5), 847–856 (2008). DOI 10.1007/s00348-008-0504-6
66. Ziskin, I.B., Adrian, R.J., Prestridge, K.: Volume segmentation tomographic particle image velocimetry. In: 9th international symposium on particle image velocimetry. Kobe, Japan (2011)